

Quantum signatures in a quadratic optomechanical heat engine with an atom in a tapered trap

MOHSEN IZADYARI,^{1,*} MEHMET ÖNCÜ,² KADIR DURAK,² AND
ÖZGÜR E. MÜSTECAPLIOĞLU^{1,3}

¹*Department of Physics, Koç University, Istanbul, 34450, Turkey*

²*Department of Physics, Özyeğin University, Istanbul, 34794, Turkey*

³*TÜBİTAK Research Institute for Fundamental Sciences, Gebze, 41470, Turkey*

*mizadyari18@ku.edu.tr

Abstract: We investigate how quantum signatures can emerge in a single atom heat engine consisting of an atom confined in a tapered trap and subject to hot and cold thermal reservoirs. A similar system was realized experimentally in Ref. [1]. We model such a system using a quadratic optomechanical model and identify an effective Otto cycle in the system's dynamics. We compare the engine's performance in the quantum and classical regimes by evaluating the power dissipated. We find that lowering the temperature is insufficient to make the single atom engine of Ref. [1] a genuine quantum-enhanced heat engine. We show that it is necessary to make the trap more asymmetric and confined to ensure that quantum correlations cause an enhancement in the power output.

© 2022 Optica Publishing Group under the terms of the [Optica Open Access Publishing Agreement](#)

1. Introduction

Quantum heat engines (QHEs) are machines harnessing thermal energy using quantum working substances [2, 3]. While the three-level maser, a quantum device that amplifies microwave radiation, was recognized as a QHE several decades ago [4], systematic studies of QHE have attracted much attention quite recently [5–36]. A pioneering experiment was the demonstration of a piston-type (Otto) engine using a single trapped ion [1]. Due to the relatively small energy gaps of the trapped ion at the involved temperatures, genuine, profound quantum effects in the single-atom piston were assumed to be non-existent. Here, we ask if it is sufficient to lower the temperature to bring the experimental setup to the quantum regime or if it is necessary to make more modifications. To answer this question, we use a higher-order, so-called quadratic, optomechanical model of the interaction between the motional degrees of freedom of the atom arising due to the tapered trap geometry of the experiment.

It was intuitively expected that an optomechanical-type mutual interaction effectively emerges when an atom is confined in a funnel-shaped trap [1]. Here, we explicitly verify this intuition, but surprisingly, we find an additional degenerate three-wave mixing type coupling. It is a well-known interaction for generating squeezed states [37–39]. After that, we explore the signatures of the quantum squeezing in the system by differentiating classical and quantum correlations via solving master and classical stochastic Langevin equations separately. In a single atom system trapped in a tapered trap, we find that quantum correlations arise by increasing coupling strength between axial and radial modes. These quantum correlations can significantly enhance the dissipated power relative to the classical correlations. According to our model, the coupling strength depends on the trap's geometry and frequencies asymmetry. So, we indicate that the dissipated power can be enhanced by increasing the trap asymmetry and reducing the trap radius. The results show that lowering the temperature of the experiment [1] per se is not sufficient to bring the single-ion engine to the quantum regime. As a result, making the trap geometry more

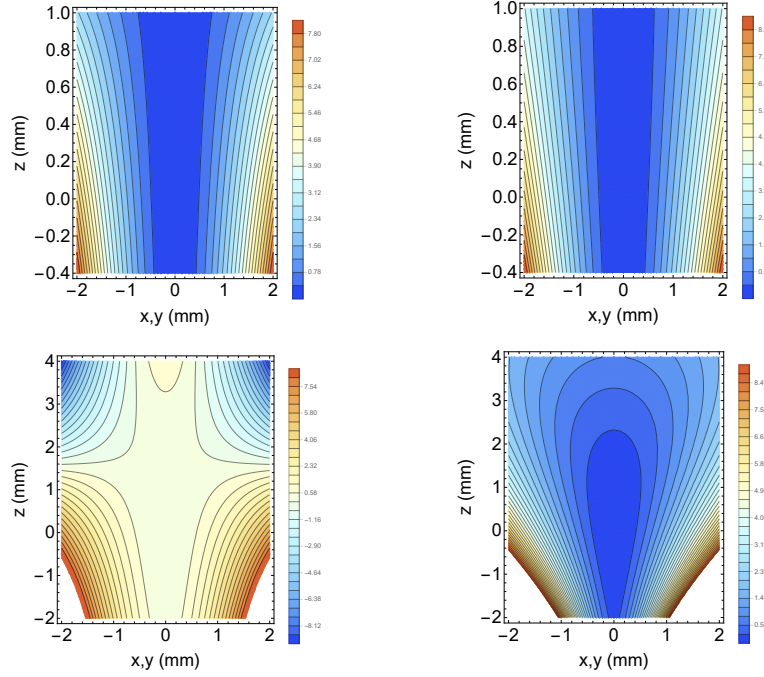


Fig. 1. Cross sections of the approximate (Left panels) and exact (Right panels) funnel-shaped potential (in units of eV) of the tapered trap geometry. The approximation requires $z \tan \theta \ll r_0$ where $\theta = 30^\circ$ is the tapered trap angle and $r_0 = 1.1$ mm is the trap radius at $z = 0$. The calculations are done for the Calcium ion of mass $m = 40u$ in atomic unit $u = 1.66 \times 10^{-27}$ kg.

asymmetric and the atom more confined at low temperatures make quantum squeezing type correlations more significant for a remarkable performance increase than the classical stochastic engine. Accordingly, we conclude that, in addition to lowering the temperature, the original single-atom heat engine setup in Ref. [1] can be converted into a genuine quantum-enhanced heat engine in a more asymmetric and confined configuration.

This paper is organized as follows. In Sec. 2, we describe our Hamiltonian model to describe the experimental ion in a tapered trap system in Ref. [1]. In Sec. 3, we investigate the dynamics of the system using the master equation approach. We identify an effective Otto cycle for the radial mode in Sec. 4. Sec. 5 compares the stochastic and quantum dissipated power outputs through the axial mode. We conclude in Sec. 6.

2. Model System

Single ion-heat engine realized in Ref. [1] consists of a Calcium ion of mass m in a tapered trap geometry. In the axial (z) direction the trap frequency is ω_z . In the directions, x , y , the trap frequencies are given by

$$\omega_\alpha = \frac{\omega_{0\alpha}}{(1 + \epsilon z)^2}, \quad (1)$$

where $\epsilon := (\tan \theta)/r_0$. Here, $r_0 = 1.1$ mm is the radius of the trap at $z = 0$ and $\theta = 30^\circ$ is the trap angle. Trap frequencies along x and y axes are given as ω_{0x} and ω_{0y} , respectively. It is found that during the heat engine operation, the ion makes axial coherent oscillations with amplitude in the order of micrometers [1]. Accordingly, we can consider $\epsilon z \ll 1$ for the description of heat

engine dynamics. In this limit, the trap potential,

$$U(x, y, z) = \frac{m}{2}(\omega_x^2 x^2 + \omega_y^2 y^2 + \omega_z^2 z^2), \quad (2)$$

can be approximated by

$$V(r, y) = \frac{m}{2}\omega_r^2 r^2(1 - gz) + \frac{m}{2}\omega_z^2 z^2, \quad (3)$$

where $r^2 = x^2 + y^2$, and $g = 4\epsilon \approx 2.1$ (1/mm). We neglected the small difference between ω_x and ω_y and replace them with the mean radial trap frequency, $\omega_r := (\omega_{0x} + \omega_{0y})/2$ [1]. The trap potential $U(x, y, z)$ (using Eq. (1) to define ω_x and ω_y) and its approximation by $V(r, z)$ are compared in Fig. 1 (right and left panels respectively). According to Fig. 1 (upper panels), the exact potential can be superseded by approximated potential for small values of z .

The trapped ion is always subject to a cooling laser yielding the effect of a cold thermal bath. An electrical white noise is applied to the radial degree of freedom for periodical heating as illustrated in Fig. 2. The heat engine system with two radial (*a*) and axial (*b*) vibrational modes (coupled by β) is shown in Fig. 2. Accordingly, two thermal baths at temperatures T_h and T_a couple to radial mode, and the axial mode is coupled to a bath at temperature T_b . The coupling between system and thermal bath at temperature T_h is periodically turned on and off. The engine cycle is examined classically in Ref. [1], which is justified for $k_B T \gg \hbar\omega_r$, where T is considered as the working temperatures of the engine. Indeed, for all temperatures of interest, including the high-temperature condition $T_c \gg \hbar\omega_r$ is satisfied. On the other hand, the particular coupling of the axial and radial degrees of freedom in Eq. (3) contains a quadratic nonlinearity in r . From the quantum mechanical point of view, such a nonlinearity could yield a quantum noise squeezing effect.

Let us express the quantum model of the center-of-mass (CM) motion, in the form

$$H_0 = \frac{P_r^2 + P_z^2}{2M} + V(r, z). \quad (4)$$

Here, P_r and P_z stand for the components of the CM momentum operator, with $P_r^2 = P_x^2 + P_y^2$. We apply the harmonic-oscillator quantization $r = (\hbar/m\omega_r)^{1/2}\hat{q}_r$, $z = (\hbar/m\omega_z)^{1/2}\hat{q}_z$, $P_r = (\hbar m\omega_r)^{1/2}\hat{p}_r$, and $P_z = (\hbar m\omega_z)^{1/2}\hat{p}_z$ with $\hat{p}_r = i(\hat{a}^\dagger - \hat{a})/\sqrt{2}$, $\hat{p}_z = i(\hat{b}^\dagger - \hat{b})/\sqrt{2}$, $\hat{q}_r = (\hat{a}^\dagger + \hat{a})/\sqrt{2}$, and $\hat{q}_z = (\hat{b}^\dagger + \hat{b})/\sqrt{2}$ to write the Hamiltonian (4) in terms of the vibrational phonon operators, (we take $\hbar = 1$)

$$\hat{H}_{\text{cm}} = \omega_r \hat{n}_r + \omega_z \hat{n}_z - \frac{\beta}{4}(\hat{a}^2 + \hat{a}^{\dagger 2} + 2\hat{a}^\dagger \hat{a} + 1)(\hat{b} + \hat{b}^\dagger), \quad (5)$$

where we have dropped the constants $\omega_r/2$ and $\omega_z/2$. $\beta \equiv g\omega_r\sqrt{\hbar/2m\omega_z}$ is the coupling coefficient of r and z degrees of freedom; $\hat{n}_r = \hat{a}^\dagger \hat{a}$, and $\hat{n}_z = \hat{b}^\dagger \hat{b}$ are the phonon number operators in r and z directions, respectively. We remark that the coupling coefficient β depends on trap geometry through the coupling constant g .

The Hamiltonian (5) can be compared to an optomechanical-like Hamiltonian, but in addition to the occupation of mode *a*, quantum squeezing-type correlations can induce additional pressure on mode-*b* to produce coherent displacement or useful work. To isolate the effects of different coupling mechanisms in Eq. (5), we simulate each of them using the separate models,

$$H_{\text{om}} = \omega_r \hat{n}_r + \omega_z \hat{n}_z - \frac{\beta}{2}\hat{a}^\dagger \hat{a}(\hat{b} + \hat{b}^\dagger), \quad (6)$$

$$H_{\text{class}} = \omega_r \hat{n}_r + \omega_z \hat{n}_z - \frac{\beta}{4}(\hat{b} + \hat{b}^\dagger), \quad (7)$$

$$H_{\text{sq}} = \omega_r \hat{n}_r + \omega_z \hat{n}_z - \frac{\beta}{4}(\hat{a}^2 + \hat{a}^{\dagger 2})(\hat{b} + \hat{b}^\dagger). \quad (8)$$

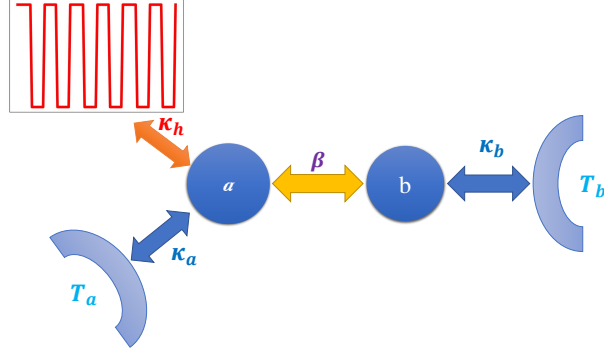


Fig. 2. Diagram of the heat engine system based on the radial (a) and axial (b) vibrational modes whose coupling is characterized by the parameter β . Radial mode is coupled to two thermal baths at temperatures T_h and T_a , where the coupling to the bath at temperature T_h is periodically turned on and off, and the axial mode is coupled to a bath at temperature T_b . The background environment common to both modes is not shown.

Eq. (6) describes a pure optomechanical coupling where only the occupation of mode- a produces pressure on mode- b . Modes are uncoupled in Hamiltonian (7), but there is still an effective classical drive on mode- b . Eq. (8) injects coherence in mode- b depending on the squeezing of mode a .

In the next section, we will simulate the system based on total Hamiltonian Eq. (5) as system A_0 , and each of the models in Eqs. (6-8) as systems A_1 , A_2 and A_3 , respectively. Let's emphasize that optomechanical coupling can not emerge per se but is always accompanied by the other classical and squeezed drive terms, and each coupling contributes with comparable or the same strengths. Our separation is artificial and only for the purpose of shedding light on the individual effects of each term on the coherent dynamics of mode- b , in particular on the work output of the single ion heat engine. We note that Ref. [24] assumes Gaussian thermal distribution to model the spatial distribution of mode- a . This description would be closer to the classical treatment of our optomechanical model of A_1 given by Eq. (6).

3. Results

In this section, we introduce the parameters we used in our simulations and describe the open quantum system dynamics of the system in terms of a master equation.

3.1. Parameters

The experiment [1] has been performed at high temperature (in the order of mK). As the usual route to the quantum regime is to reduce the temperature, we consider the temperature in the order of the μK . However, we find that lowering the temperature is insufficient to see the system's quantum effects. It is required to demonstrate the system can harness more power than its stochastic counterpart to be classified as a genuine quantum (enhanced) heat engine [40]. In addition to reducing the temperature, increasing β plays a crucial role in achieving clear signatures of quantum enhancement in the heat engine operation with a single ion in a tapered trap. It is necessary to exploit quantum squeezing type correlations to enhance power output relative to the case where there are only classical correlations.

In the following, we take $T_h = 166 \mu\text{K}$ and $T_a = T_b = 4 \mu\text{K}$ while we suppose the atom's initial temperature is $T_0 = 10 \mu\text{K}$. Also, the radial and axial frequencies are taken $\omega_r/2\pi = 1$

MHz and $\omega_z/2\pi = 50$ kHz, respectively. According to the definition of the coupling coefficient ($\beta \propto \tan \theta/r_0$), we consider high trap asymmetry by taking $\theta = \pi/4$ and considering more confined traps with $r_0 \lesssim 20 \mu\text{m}$ [41, 42] to make the coupling stronger. For example, for $r_0 \approx 2 \mu\text{m}$ and using the aforementioned parameters, we find $\beta/2\pi = 100$ kHz. We emphasize that these parameters are not arbitrary but taken as an example from a range of values for which the temperatures are sufficiently low and squeezing type coupling is sufficiently large to get into the quantum enhanced regime of engine operation.

The dissipation rates of mode a to the cold and hot baths are considered to be $\kappa_a/2\pi = \kappa_h/2\pi = 200$ kHz, where κ_h is taken as a time-dependent square wave $\kappa_h(t) := \kappa_h u(t)$. The time-dependent part is $u(t) = 1$ for the heating and otherwise $u(t) = 0$. Also, the dissipation rate of mode b to the cold bath is $\kappa_b/2\pi = 50$ kHz.

3.2. The dynamics of the system

According to Eq. (5), the model effectively describes two nonlinearly coupled single-mode resonators. We assume a microwave white noise and a cooling laser are applied to the mode a , as shown in the experiment of Ref. [1]. This continuous electrical noise and cooling laser plays the roles of two cold and heat baths at temperatures T_a and T_h such that $T_h > T_a$. An extra cooling laser beam is introduced to mode b to keep the axial mode's oscillations in control by tuning its parameters on purpose to get a limit cycle at temperature T_b . The background environment with temperature T_0 has been ignored during the dynamics by assuming the coupling coefficient of background environment with mode b and a less than κ_j where $j \in \{h, a, b\}$ [43]. The dynamics of the density matrix ρ of the two-resonator system is determined by the master equation [44–46]

$$\begin{aligned} \frac{d\rho}{dt} = & -i[\hat{H}_\lambda, \rho] \\ & + \kappa_a(\bar{n}_a + 1)D[\hat{a}] + \kappa_a\bar{n}_aD[\hat{a}^\dagger] \\ & + \kappa_h(t)(\bar{n}_h + 1)D[\hat{a}] + \kappa_h(t)\bar{n}_hD[\hat{a}^\dagger] \\ & + \kappa_b(\bar{n}_b + 1)D[\hat{b}] + \kappa_b\bar{n}_bD[\hat{b}^\dagger], \end{aligned} \quad (9)$$

where $\lambda = \text{cm, om, class, sq}$ represents different models and $D[\hat{a}] = (1/2)(2\hat{a}\rho\hat{a}^\dagger - \hat{a}^\dagger\rho\hat{a} - \rho\hat{a}^\dagger\hat{a})$ refers to the Lindblad dissipator superoperators with $\hat{a} = \hat{a}, \hat{b}$. Mean number of phonons in mode a and b at the bath temperature T_u and T_b is denoted by \bar{n}_u with $u \in \{a, h\}$ and \bar{n}_b , given by the Planck distribution (we take $k_B = 1$)

$$\begin{aligned} \bar{n}_u &= \frac{1}{\exp(\omega_r/T_u) - 1}, \\ \bar{n}_b &= \frac{1}{\exp(\omega_z/T_b) - 1}. \end{aligned} \quad (10)$$

We assume that before the cooling and heating lasers are applied, the ion and its vibrational modes are in thermal equilibrium with the background thermal environment at temperature T_0 . Initial state then can be expressed as a canonical thermal (Gibbs) state such that

$$\rho(0) = \frac{1}{\text{Tr}[e^{-\hat{H}_\lambda/T_0}]} e^{-\hat{H}_\lambda/T_0}, \quad (11)$$

and the initial states of the vibrational modes are determined by the reduced density matrices $\rho_b(0) = \text{Tr}_b(\rho(0))$ and $\rho_a(0) = \text{Tr}_a(\rho(0))$. We solve the master equation to determine $\rho(t)$ for the given $\rho(0)$ using Python programming language and an open source quantum optics package QuTiP [47]. Taking the partial trace of $\rho(t)$ over the degrees of freedom of mode- a , we find the reduced state of the mode- b such that $\rho_b(t) = \text{Tr}_a[\rho(t)]$. Time dependence of the mean number

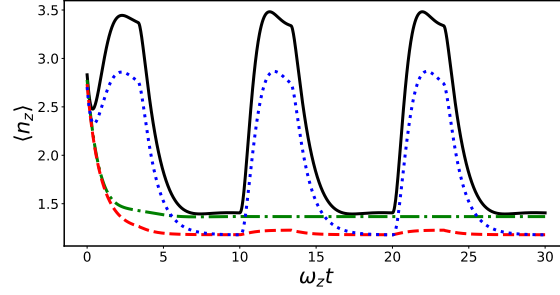


Fig. 3. Dynamics of the mean number of vibrational phonons $\langle n_z \rangle$ in modes b where time is scaled with ω_z . The parameters used in the plots are taken to be $\omega_r/2\pi = 1$ MHz, $\omega_z/2\pi = 50$ kHz, $\bar{n}_h = 3$, and $\beta/2\pi = 100$ kHz. The solid black, dotted blue, dash-dotted green, and dashed red lines show the evolution of $\langle n_z \rangle$ under the models A_0 , A_1 , A_2 , and A_3 , respectively.

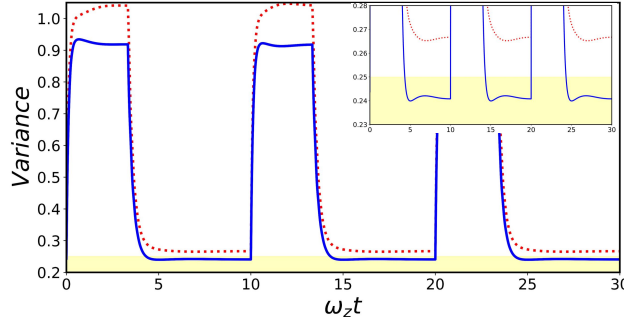


Fig. 4. The time evolutions of the variances of the quadratures $(\langle \Delta \hat{q}_r \rangle)^2$ (red dotted line) and $(\langle \Delta \hat{p}_r \rangle)^2$ (blue solid line) of the radial mode. The inset magnifies the squeezing region where Variance $< 1/4$.

of vibrational phonons in mode- b is evaluated by $\langle \hat{n}_z \rangle = \text{Tr}(\rho_b(t) \hat{b}^\dagger \hat{b})$. Similar calculations give dynamics of $\langle \hat{n}_r \rangle$, too.

The evolutions of $\langle \hat{n}_z \rangle$ for the four models A_0 to A_3 are shown in Fig. 3. Since all the models A_0 to A_3 have different Hamiltonians, the initial conditions differ. Nevertheless, the differences in the initial value of $\langle \hat{n}_z \rangle$ are too small to be visible in Fig. 3. Among all the terms in the overall interaction A_0 , optomechanical type coupling A_1 is the only mechanism to increase the axial mode population. However, despite the qualitative agreement, A_1 per se cannot quantitatively explain the $\langle \hat{n}_z \rangle$ behavior. While the squeezing term A_3 cannot directly populate $\langle \hat{n}_z \rangle$; it plays a subtle role to increase $\langle \hat{n}_z \rangle$ beyond what is possible solely by A_1 .

Intuitively, the effect of squeezing-type terms A_3 in A_0 can be interpreted as an enhancement of vibrational radial pressure on the axial mode. When A_3 terms are present, the number of radial vibrational phonons during the heating stage is expected to increase so that the optomechanical-like coupling A_1 in A_0 can yield higher $\langle \hat{n}_z \rangle$. The more radial phonons cause stronger pressure on the axial mode to transfer more energy or power. To appreciate how the quantum character of the modes enters into this picture, let us look at the dynamics of $\langle \hat{n}_z \rangle$ according to the master

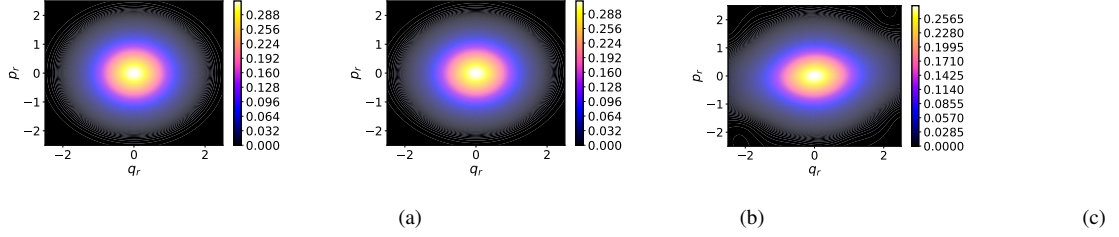


Fig. 5. Colour online) (a)-(c) The Wigner functions in the p_r, q_r field quadrature phase space of the radial mode plotted for (a) $\beta/2\pi = 10$ kHz, (b) $\beta/2\pi = 100$ kHz, (c) $\beta/2\pi = 200$ kHz. The other system parameters are $\omega_r/2\pi = 1$ MHz, $\omega_z/2\pi = 50$ kHz.

equationn (9)

$$\frac{d}{dt}\langle\hat{n}_z\rangle = \frac{\beta}{\sqrt{2}}(\langle\hat{q}_r^2, \hat{p}_z\rangle + \langle\hat{q}_r^2\rangle\langle\hat{p}_z\rangle) - \kappa_b(\langle\hat{n}_z\rangle - \bar{n}_b), \quad (12)$$

where $\langle\hat{q}_r^2, \hat{p}_z\rangle := \langle\hat{q}_r^2, \hat{p}_z\rangle - \langle\hat{q}_r^2\rangle\langle\hat{p}_z\rangle$ is a quantum correlation function between the radial and axial modes. The dissipated power output of the engine is determined by $P_{\text{dis}} = \omega_z \kappa_b (\langle\hat{n}_z\rangle - \bar{n}_b)$, which measures the net flux of energy dissipated into the environment [48]. In order to produce more power than a stochastic engine that can only have classical correlations, it is necessary for us to ensure that the system has strong quantum correlations associated with the second moment of the displacement of the radial mode. Quantum character of the $\langle\hat{q}_r^2\rangle$ can be examined in terms of the quadrature variances of the radial mode

$$(\langle\Delta\hat{q}_r\rangle)^2 = \text{Tr}[\rho_a \hat{q}_r^2] - (\text{Tr}[\rho_a \hat{q}_r])^2, \quad (13)$$

$$(\langle\Delta\hat{p}_r\rangle)^2 = \text{Tr}[\rho_a \hat{p}_r^2] - (\text{Tr}[\rho_a \hat{p}_r])^2, \quad (14)$$

where $\rho_a(t) = \text{Tr}_b[\rho(t)]$ is the reduced density matrix of the radial mode. When a quadrature variance is less than its vacuum value of $1/4$, the state is said to be quadrature squeezed.

The time evolutions of $(\langle\Delta\hat{q}_r\rangle)^2$ (red dotted line) and $(\langle\Delta\hat{p}_r\rangle)^2$ (blue solid line) are shown in Fig. 4. The yellow shaded area, where Variance $< 1/4$, in Fig. 4 indicates that the radial mode starts each cycle in a squeezed thermal state. Fig. 5 plots the Wigner functions of the radial mode for different β , at the same scaled time after thermalization of the system, when the system dynamics is governed by the full model A_0 . Wigner function of a thermal state in the quadrature phase space has circular contours, which are changed to ellipses due to quadrature squeezing. In the Fig. 5, we show that although the quadrature phase space of radial mode has circular contours for small β (Fig. 5 (a)), it becomes to ellipses contours by enhancing β (figs. 5 (b,c)). So, for small β , the eccentricity is almost zero, and the squeezing is negligible even at low temperatures. Accordingly, the dissipated power of the engine will be dominated and determined by the classical correlations only. On the other hand, for large values of β , second order moments of the displacement operator should be treated quantum mechanically in Eq. 12 and hence to the calculation of the dissipated power. We present explicit calculation of P_{dis} for both quantum and classical stochastic treatments in Sec. 5.

4. Effective Otto Cycle For the Radial Mode

For a single ion in an asymmetrical Paul trap [1], the hot bath is simulated by the external white electric-field noise. The cold bath interaction is realized by exposing the ion to the laser cooling beam. According to [1, 29], the cooling laser is kept on during the process. Despite the

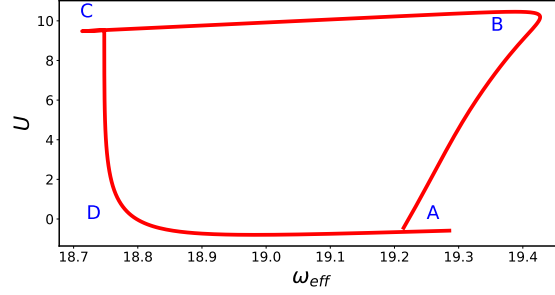


Fig. 6. Effective energy-frequency diagram of the radial mode a by considering the dependence of the mean effective energy U to the effective frequency ω_{eff} (in units of $\hbar\omega_z$).

continuous coupling to the heat baths, we can identify an Otto engine cycle in our model. We consider the mode a as the working substance and treat the mode b as the engine's flywheel where the work is stored. We replace the flywheel displacement $q_z = \langle \hat{b} + \hat{b}^\dagger \rangle$ as a number in model A_0 . The reduced semi-quantum model describes a squeezed oscillator Hamiltonian for mode a , whose diagonalization by the Bogoluibov transformation (see A.) yields an effective frequency of ω_{eff} , and the effective mean energy can be defined as $U = \langle H'_{\text{cm}} \rangle$.

The Otto engine is identified in Fig. 6 with four steps [29].

(A→B) Hot isochore: the effective trapping frequency (ω_{eff}) is kept constant at ω_h while contacting with hot bath at temperature T_h . The thermalization will be done after a time of τ_h .

(B→C) Adiabatic expansion: The atom evolves in the trapping potential while isolated from the hot bath. After a time τ_z , the effective frequency will be changed from ω_h to ω_c , and work will be done by considering the displacement in the axial direction.

(C→D) Cold isochore: the effective frequency remains in ω_c , and the cold bath with temperature T_c is contacted with the system for a time τ_c .

(D→A) Adiabatic compression: the effective frequency returns to the initial frequency another time τ_z in the last step.

The time scales can be considered by $\tau_h \approx \tau_c < \tau_z$. An effective, finite-time (non-ideal) Otto cycle (ABCD) is defined in the diagram (Fig. 6) where we plot dependence of U on ω_{eff} in the steady state at $\bar{n} = 3$.

4.1. Performance of the engine

We have seen that the engine operates by converting the thermal energy harvested by the radial mode into coherent oscillations of the axial vibrational mode. We can envision the vibrational mode as the work reservoir storing coherent energy and examine the engine cycle for the radial mode. For that aim, let's consider a semi-classical model of the vibrational interaction by replacing the coherent axial mode operators, in particular q_z operator in the vibrational coupling with a c-number, which is its expectation value. After that, we can apply the Bogoluibov transformation (as described in A) to the effective semi-classical model, which yields a simple uncoupled quantum oscillator model. Accordingly, we conclude that the vibrational modes, particularly the radial mode, are Gaussian states under the semi-classical model. More specifically, the radial mode is a Gibbsian (thermal equilibrium) Gaussian state for which a simple Von-Neumann entropy expression can be derived in the form [43]

$$S = (1 + \langle \hat{n}_c \rangle) \ln(1 + \langle \hat{n}_c \rangle) - \langle \hat{n}_c \rangle \ln(\langle \hat{n}_c \rangle). \quad (15)$$

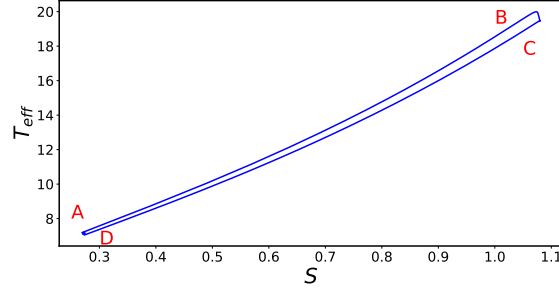


Fig. 7. T-S diagram of the mode a which closely resembles that of an Otto engine (in units of $\hbar\omega_z$)

The effective temperature of the radial mode Gibbsian state is given by

$$T_{\text{eff}} = \omega_{\text{eff}} / \ln(1 + 1/\langle \hat{n}_c \rangle). \quad (16)$$

Here, the $\langle \hat{n}_c \rangle$ comes from the diagonalized form of radial mode in Hamiltonian employing Bogoliubov transformation (A).

The temperature-entropy $T - S$ diagram is plotted in Fig. ?? which closely resembles an Otto engine. The potential work output can be obtained by calculating the area of the T-S diagram. We approximate the work from the T-S diagram, and the net work is estimated by $W \approx 0.22 \hbar\omega_z \approx 7.3 \times 10^{-30}$ joules. The Power can be calculated by dividing work by the cycle time $T = 20 \times 2\pi/\omega_z$ as $P \approx 2.9 \times 10^{-27}$ Watts. The determined heat intake of mode a is $Q_{\text{in}} \approx 3 \times 10^{-28}$ joules, and therefore the efficiency is $\eta \approx 2.4\%$.

The coupling coefficient β in Hamiltonian (5) plays an essential role in producing work and achieving higher efficiency, which can be done by revising the trap's geometry in the experiment [1]. Engine performance improves by applying the quantum correlations, which are significant only for much higher coupling regimes and at low temperatures. According to the definition of $\beta \propto 1/r_0$, we can increase β by lowering the trap's radius r_0 . As we argued in Sec. 3.1, sufficiently large β can be achieved by reducing the trap's radius to the micrometer scale. Fig. 8 shows the dependence of the extracted work, determined by the area of the $T - S$ diagram, on r_0 . Here, θ , radial, and axial frequencies are kept constant so that β increases with r_0 . It can be pointed out that the work output increases strongly in tightly confined tapered traps. We remark, however, that increasing the coupling coefficient β is limited in our treatment where we use a local optomechanical master equation, which requires β to be smaller than the radial frequency [49].

5. Classical vs Quantum Heat Engine Regimes

The previous section identifies an effective Otto cycle by treating the radial mode as a working fluid and assuming the coherent displacements of axial mode are classical. This treatment allows us to use conventional thermodynamic cycle diagrams in terms of mean effective energy, effective temperature, effective frequency (spatial-like parameter), and entropy for our reduced quantum oscillator model for the radial mode. In this case, the potential work output of the effective Otto cycle is computed from the $T - S$ diagram. The missing piece of this engine picture is the flywheel, which is the axial mode. The work is translated to the piston (axial) mode, and it is determined in terms of the dissipated power through the axial mode, which we will calculate in the present section. Dissipated power is essentially determined with the population of the axial

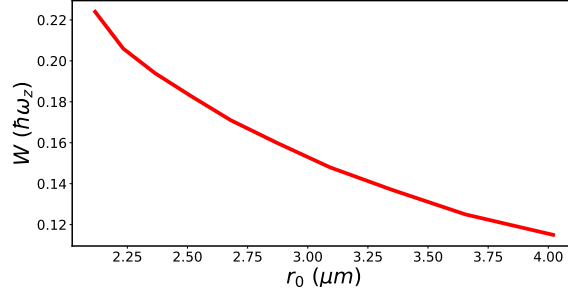


Fig. 8. Extracted work W (in unit of $\hbar\omega_z$) versus trap's radius r_0 (μm) where radial and axial frequencies are constant ($\omega_r/2\pi = 1$ MHz, and $\omega_z/2\pi = 50$ kHz) and $\theta = \pi/4$.

mode (mean number of axial phonons). As we have seen in Sec. 3, the dynamical equation of the mean number of axial phonons includes a quantum correlator term, which can be significant on top of classical correlations when quantum squeezing is present and can enhance the dissipated power. When there are only classical correlations, we solve the Langevin equations to determine the mean number of axial phonons. In addition, we determine the mean number of axial phonons from the quantum master equation as well. Using these two methods, we will determine the mean number of phonons to be substituted to the same dissipated power formula to compare the classical and quantum dissipated power outputs with each other.

To compare the quantum engine with its classical counterpart, we follow the standard method of neglecting the non-commutative character of the quantum operators (for example, position and momentum operators). In the optomechanical engine models, they are replaced with c-numbers, $\langle\hat{a}\rangle \rightarrow v_r$ and $\langle\hat{b}\rangle \rightarrow v_z$ [43, 48]. The Heisenberg equations of motion are then changed to classical Langevin equations, which further include the stochastic noise terms describing the classical models of the heat baths in the form

$$\begin{aligned}
\dot{v}_r &= -i \left(\omega_r v_r - \frac{\beta}{2} (v_r^* + v_r)(v_z + v_z^*) \right) \\
&\quad - \frac{\kappa_r + \kappa_h}{2} v_r + \xi_h(t) + \xi_r(t), \\
\dot{v}_z &= -i \left(\omega_z v_z - \frac{\beta v_z}{4} (v_r^2 + v_r^{*2} + 2v_r v_r^* + 1) \right) \\
&\quad - \frac{\kappa_b}{2} v_z + \xi_z(t).
\end{aligned} \tag{17}$$

Here $\xi_k(t)$ presents time dependent delta-correlated and temperature dependent stochastic noise terms where $k = r, z, h$ [43, 48].

Defining the field quadratures X_i, Y_i as $v_i = 1/\sqrt{2}(X_i + iY_i)$, and writing the noise parameters as $\xi_i = 1/\sqrt{2}(\xi_x^i + i\xi_y^i)$ where $i = r, z$ we can simulate the equations as:

$$\begin{aligned}
dX_r &= \left(\omega_r Y_r - \frac{\kappa_a + \kappa_h}{2} X_r \right) dt + dW_x^h + dW_x^a, \\
dY_r &= \left(-\omega_r X_r + \sqrt{2}\beta X_r X_z - \frac{\kappa_a + \kappa_h}{2} Y_r \right) dt + dW_y^h + dW_y^a, \\
dX_z &= \left(\omega_z Y_z - \frac{\kappa_b}{2} X_z \right) dt + dW_x^b, \\
dY_z &= \left(-\omega_z X_z + \frac{\sqrt{2}\beta}{4} (4X_r^2 + 1) - \frac{1}{2}\kappa_b Y_z \right) dt + dW_y^b.
\end{aligned} \tag{18}$$

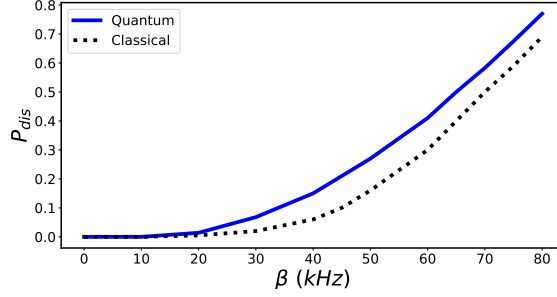


Fig. 9. The maximum dissipated power (in units of $\hbar\omega_z$) concerning coupling constant β (in units of kHz). The black dashed and solid blue curves show the results of classical and quantum simulations, respectively.

Here, $dW^i = 1/\sqrt{2}(dW_x^i + idW_y^i)$ where $\xi_k^i dt = dW_k^i$, with $k = x, y$, is the Wiener process with width $\sqrt{\kappa_i \bar{n}_i dt}$.

We solve these equations to determine the mean number of phonons,

$$\langle \hat{n}_z \rangle = \frac{1}{2}(X_z^2 + Y_z^2), \quad (19)$$

which is then used to determine the dissipated power. The calculation is then repeated using the quantum master equation instead of the Langevin equations. Fig. 9 shows the maximum dissipated power output of classical and quantum calculations versus β . It reveals that the quantum model enables power outputs that greatly exceed the power of stochastic engines for large β , which identifies the regime in which the system can be classified as a genuine quantum heat engine (according to the criteria in Ref. [40]).

The quantum correlation contributions to the engine performance are negligibly small in the single-ion heat engine experiment [1], and it should be classified as a classical heat engine even at low temperatures according to the criteria of Ref. [40]. It is necessary to modify the setup by increasing the asymmetry of the tapered trap and decreasing the trap's radius (to increase β) to bring the single-ion engine of Ref. [1] to the domain of quantum heat engines. According to our calculations, the dissipated power output of the engine overcomes the stochastic classical power output with the help of quantum correlations when $\beta \geq 20$ kHz. As an example, to reach this condition by using the parameters defined in Sec. 3 we can use $\theta = 45^\circ$ and $r_0 \leq 10 \mu\text{m}$.

6. Conclusion

In summary, we examined the single-atom heat engine using the asymmetric trap configuration of experiment Ref. [1] employing a quadratic optomechanical model. In our model, the working fluid mode (radial mode) was simultaneously driven by the contribution of optomechanical, classical, and squeezed terms. We clarified the effects of the coherent and squeezing couplings on the engine's operation beyond the standard optomechanical coupling. Furthermore, it was found that the coupling coefficient β plays a critical role in increasing quantum correlations contribution and enables power outputs that greatly exceed the power of stochastic engines. We showed that the engine should perform in a high coupling and low-temperature regime to benefit from the quantum correlations. According to our calculations, the quantum character of the second order moments of the displacement operator emerges by increasing β . In the strong coupling regime, the radial mode is in a thermal squeezed state, and as a result, the system treats quantum mechanically. The coupling coefficient depends on the trap's geometry and the

frequencies asymmetry, so adjusting the trap's geometry asymmetry and reducing the trap's radius can increase the efficiency and work of the engine. We concluded that a single atom heat engine in a more confined and asymmetric trap operates in the quantum regime where the dissipated power is more significant than its classical counterpart with only classical stochastic correlation.

Acknowledgments. This work was supported by the Scientific and Technological Research Council of Turkey (TUBITAK) with project number 119F200.

A. Effective entropy and temperature of the working mode a

To diagonalize the Hamiltonian (5), we first replace the q_z operator with its expectation value. The new effective semi-quantum model describes the radial mode as the working fluid of the engine. The effective reduced model is a quadratic form and it can be diagonalized using the Bogoliubov transformations

$$\hat{a} = \hat{c} \cosh x + \hat{c}^\dagger \sinh x, \quad (20)$$

$$\hat{a}^\dagger = \hat{c} \sinh x + \hat{c}^\dagger \cosh x. \quad (21)$$

Here, $\tanh 2x = \beta q_z / (2\omega_r - \beta q_z)$. The diagonalized Hamiltonian becomes

$$\begin{aligned} \hat{H}'_{cm} = & \omega_{\text{eff}} \hat{n}_c + \omega_z \hat{n}_z + \omega_r \sinh^2 x \\ & - \frac{\beta q_z}{2} (\sinh 2x + \cosh 2x), \end{aligned} \quad (22)$$

where an effective frequency ω_{eff} is defined to be

$$\omega_{\text{eff}} = (\omega_r - \frac{\beta q_z}{2}) \cosh 2x - \frac{\beta q_z}{2} \sinh 2x. \quad (23)$$

References

1. J. Roßnagel, S. T. Dawkins, K. N. Tolazzi, O. Abah, E. Lutz, F. Schmidt-Kaler, and K. Singer, "A single-atom heat engine," *Science* **352**, 325–329 (2016).
2. J. E. Geusic, E. O. Schulz-DuBios, and H. E. D. Scovil, "Quantum equivalent of the *Carnot* cycle," *Phys. Rev.* **156**, 343 (1967).
3. R. Kosloff and A. Levy, "Quantum heat engines and refrigerators: Continuous devices," *Annu. Rev. Phys. Chem.* **65**, 365–393 (2014).
4. H. E. D. Scovil and E. O. Schulz-DuBois, "Three-level masers as heat engines," *Phys. Rev. Lett.* **2**, 262 (1959).
5. S. T. Dawkins, O. Abah, K. Singer, and S. Deffner, *Single Atom Heat Engine in a Tapered Ion Trap* (Springer, 2019).
6. T. D. Kieu, "The second law, maxwell's demon, and work derivable from quantum heat engines," *Phys. Rev. Lett.* **93**, 140403 (2004).
7. H. T. Quan, P. Zhang, and C. P. Sun, "Quantum heat engine with multilevel quantum systems," *Phys. Rev. E* **72**, 056110 (2005).
8. H. T. Quan, Y. xi Liu, C. P. Sun, and F. Nori, "Quantum thermodynamic cycles and quantum heat engines," *Phys. Rev. E* **76**, 031105 (2007).
9. M. O. Scully, K. R. Chapin, K. E. Dorfman, M. B. Kim, and A. Svidzinsky, "Quantum heat engine power can be increased by noise-induced coherence," *Proc. Natl. Acad. Sci.* **108**, 15097 (2011).
10. F. Altintas, A. U. C. Hardal, and O. E. Mustecaplioglu, "Quantum correlated heat engine with spin squeezing," *Phys. Rev. E* **90**, 032102 (2014).
11. O. Abah, J. Roßnagel, G. Jacob, S. Deffner, F. Schmidt-Kaler, K. Singer, and E. Lutz, "Single-ion heat engine at maximum power," *Phys. Rev. Lett.* **109**, 203006 (2012).
12. C. Bergenfeldt, P. Samuelsson, B. Sothmann, C. Flindt, and M. Buttiker, "Hybrid microwave-cavity heat engine," *Phys. Rev. Lett.* **112**, 076803 (2014).
13. J. Roßnagel, O. Abah, F. Schmidt-Kaler, K. Singer, and E. Lutz, "Nanoscale heat engine beyond the *Carnot* limit," *Phys. Rev. Lett.* **112**, 030602 (2014).
14. F. Altintas, A. U. C. Hardal, and O. E. Mustecaplioglu, "Rabi model as a quantum coherent heat engine: From quantum biology to superconducting circuits," *Phys. Rev. A* **91**, 023816 (2015).
15. K. Zhang and W. Zhang, "Quantum optomechanical straight-twin engine," *Phys. Rev. A* **95**, 053870 (2017).

16. M. T. Naseem and O. E. Mustecaplıoğlu, "Quantum heat engine with a quadratically coupled optomechanical system," *J. Opt. Soc. Am. B* **36**, 3000 (2019).
17. G. Barontini and M. Paternostro, "Ultra-cold single-atom quantum heat engines," *New J. Phys.* **21**, 063019 (2019).
18. J. Wang, Z. Wu, and J. He, "Quantum otto engine of a two-level atom with single-mode fields," *Phys. Rev. E* **85**, 041148 (2012).
19. P. G. Steeneken, K. L. Phan, M. J. Goossens, G. E. J. Koops, G. J. A. M. Brom, C. van der Avoort, and J. T. M. van Beek, "Piezoresistive heat engine and refrigerator," *Nat. Phys.* **7**, 354 (2011).
20. K. Kaur, V. Singh, J. Ghai, S. Jena, and Özgür E. Müstecaplıoğlu, "Unified trade-off optimization of a three-level quantum refrigerator," *Phys. A* **576**, 125892 (2021).
21. A. Ghosh, V. Mukherjee, W. Niedenzu, and G. Kurizki, "Are quantum thermodynamic machines better than their classical counterparts?" *Eur. Phys. J. Spec. Top.* **227**, 2043–2051 (2019).
22. J. Brantut, C. Grenier, J. Meineke, D. Stadler, S. Krinner, C. Kollath, T. Esslinger, and A. Georges, "A thermoelectric heat engine with ultracold atoms," *Science* **342**, 713 (2013).
23. V. Blickle and C. Bechinger, "Realization of a micrometre-sized stochastic heat engine," *Nat. Phys.* **8**, 143 (2012).
24. T. Hugel, N. B. Holland, A. Cattani, L. Moroder, M. Seitz, and H. E. Gaub, "Single-molecule optomechanical cycle," *Science* **296**, 1103 (2002).
25. I. A. Martinez, E. Roldan, L. Dinis, D. Petrov, J. M. R. Parrondo, and R. A. Rica, "Brownian *Carnot* engine," *Nat. Phys.* **12**, 67 (2016).
26. Y. Zhang, "Optimization performance of quantum otto heat engines and refrigerators with squeezed thermal reservoirs," *Phys. A* **559**, 125083 (2020).
27. H. Naseri-Karimvand, B. Lari, and H. Hassanabadi, "Non-markovianity and efficiency of a q-deformed quantum heat engine," *Phys. A* **598**, 127408 (2022).
28. H. J. Metcalf and P. van der Straten, *Laser Cooling and Trapping* (Springer, 1999).
29. A. Levy, M. Göb, B. Deng, K. Singer, E. Torrontegui, and D. Wang, "Single-atom heat engine as a sensitive thermal probe," *New J. Phys.* **22**, 093020 (2020).
30. A. Levy, L. Diósi, and R. Kosloff, "Quantum flywheel," *Phys. Rev. A* **93**, 052119 (2016).
31. D. V. Lindenfels, O. Gräb, C. T. Schmiegelow, V. Kaushal, J. Schulz, M. T. Mitchison, J. Goold, F. Schmidt-Kaler, and U. G. Poschinger, "Spin heat engine coupled to a harmonic-oscillator flywheel," *Phys. Rev. Lett.* **123**, 080602 (2019).
32. J. Sheng, C. Yang, and H. Wu, "Realization of a coupled-mode heat engine with cavity-mediated nanoresonators," *arXiv* **2110.13022** (2021).
33. M. Xu, J. T. Stockburger, G. Kurizki, and J. Ankerhold, "Minimal model of a quantum heat engine in a bandgap environment," *arXiv* **2109.12224** (2021).
34. D. Gelbwaser-Klimovsky and G. Kurizki, "Work extraction from heat-powered quantized optomechanical setups," *Sci. Rep.* **5**, 7809 (2015).
35. X. Huang, Q. Sun, D. Guo, and Q. Yu, "Quantum otto heat engine with three-qubit xxz model as working substance," *Phys. A* **491**, 604–612 (2018).
36. X. He, J. He, and J. Zheng, "Thermal entangled quantum heat engine," *Phys. A* **391**, 6594–6600 (2012).
37. G. Milburn and D. F. Walls, "Production of squeezed states in a degenerate parametric amplifier," *Opt. Commun.* **39**, 401 (1981).
38. L. A. Lugiato and G. Strini, "Production of squeezed states in a degenerate parametric amplifier," *Opt. Commun.* **41**, 67 (1982).
39. B. Yurke, "Use of cavities in squeezed-state generation," *Phys. Rev. A* **29**, 408 (1984).
40. R. Uzdin, A. Levy, and R. Kosloff, "Equivalence of quantum heat machines, and quantum-thermodynamic signatures," *Phys. Rev. X* **5**, 031044 (2015).
41. T. Decker, Y. Zheng, and A. R. et al., "A microscale planar linear ion trap mass spectrometer," *Spectrometer. J. Am. Soc. Mass Spectrom* **30**, 482–488 (2019).
42. P. F. H. et al., "Positioning of the rf potential minimum line of a linear paul trap with micrometer precision," *J. Phys. B: At. Mol. Opt. Phys.* **42**, 154008 (2009).
43. A. U. C. Hardal, N. Aslan, C. M. Wilson, and O. E. Mustecaplıoğlu, "Quantum heat engine with coupled superconducting resonators," *Phys. Rev. E* **96**, 062120 (2017).
44. H. Breuer and F. Petruccione, *The Theory of Open Quantum Systems* (Oxford, 2007).
45. M. O. Scully and M. S. Zubairy, *Quantum Optics* (Cambridge University Press, 1997).
46. J. M. Fink, L. Steffen, P. Studer, L. S. Bishop, M. Baur, R. Bianchetti, D. Bozyigit, C. Lang, S. Filipp, P. J. Leek, and A. Wallraff, "Quantum-to-classical transition in cavity quantum electrodynamics," *Phys. Rev. Lett.* **105**, 163601 (2010).
47. J. Johansson, P. Nation, and F. Nori, "Qutip 2: A python framework for the dynamics of open quantum systems," *Comput. Phys. Commun.* **184**, 1234–1240 (2013).
48. A. Mari, A. Farace, and V. Giovannetti, "Quantum optomechanical piston engines powered by heat," *J. Phys. B: At. Mol. Opt. Phys.* **48**, 175501 (2015).
49. M. T. Naseem, A. Xuereb, and Özgür E. Müstecaplıoğlu, "Thermodynamic consistency of the optomechanical master equation," *Phys. Rev. A* **98**, 052123 (2018).